Short Article

Developmental Cell

Architecture and Characteristics of Bacterial Nanotubes

Graphical Abstract

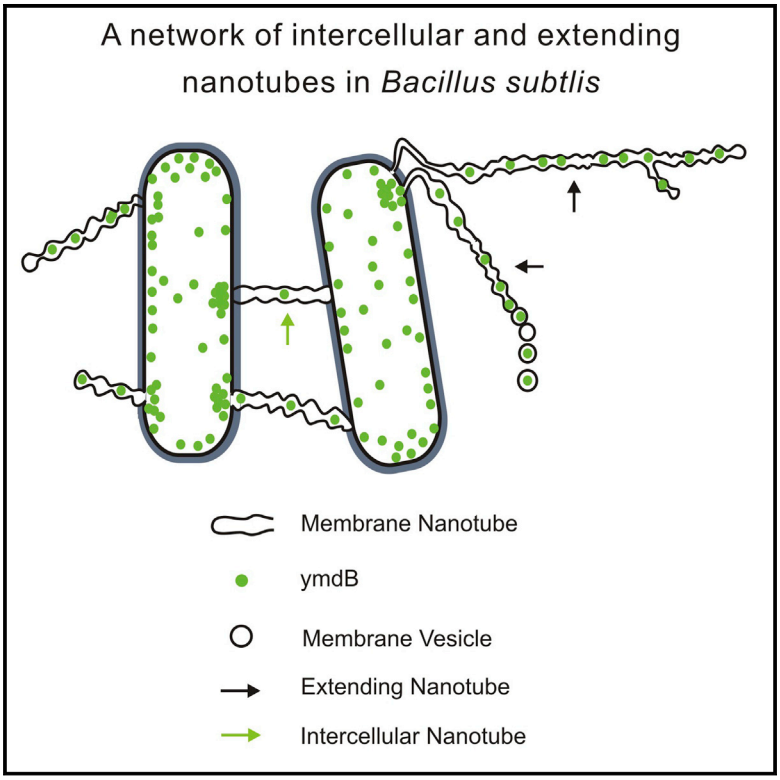

Highlights

- At low cell density, nanotubes exist as both intercellular and extending tubes
- Nanotubes are formed in the course of minutes, displaying rapid movements
- Nanotubes are composed of chains of continuous membranous segments
- YmdB is required for both nanotube production and intercellular molecular trade

Authors

Gyanendra P. Dubey, Ganesh Babu Malli Mohan, Anna Dubrovsky, ..., Eilon Sherman, Ohad Medalia, Sigal Ben-Yehuda

Correspondence

sigalb@ekmd.huji.ac.il

In Brief

Dubey et al. report that bacterial nanotubes exist as intercellular and as elongated extending tubes, with the latter dramatically expanding the cell surface. They found that nanotubes are composed of constricted lipid segments, having a continuous lumen, and identified a phosphodiesterase required for nanotube formation and intercellular molecular exchange.

Dubey et al., 2016, Developmental Cell *36*, 453–461
February 22, 2016
http://dx.doi.org/10.1016/j.devcel.2016.01.013

Developmental Cell
Short Article

Architecture and Characteristics of Bacterial Nanotubes

Gyanendra P. Dubey,[1,6] Ganesh Babu Malli Mohan,[1,6] Anna Dubrovsky,[2] Triana Amen,[3] Shai Tsipshtein,[4] Alex Rouvinski,[1,7] Alex Rosenberg,[1] Daniel Kaganovich,[3] Eilon Sherman,[4] Ohad Medalia,[2,5] and Sigal Ben-Yehuda[1,*]
[1]Department of Microbiology and Molecular Genetics, Institute for Medical Research Israel-Canada, The Hebrew University-Hadassah Medical School, The Hebrew University of Jerusalem, POB 12272, Jerusalem 91120, Israel
[2]Department of Biochemistry, University of Zurich, Winterthurerstrasse 190, 8057 Zurich, Switzerland
[3]Department of Cell and Developmental Biology, Alexander Silberman Institute of Life Sciences, The Hebrew University of Jerusalem, Jerusalem 91904, Israel
[4]Racah Institute of Physics, The Hebrew University of Jerusalem, Jerusalem 91904, Israel
[5]Department of Life Sciences and the National Institute for Biotechnology in the Negev, Ben-Gurion University of the Negev, Beer-Sheva 84120, Israel
[6]Co-first author
[7]Present address: Unité de Virologie Structurale, Département de Virologie, Institut Pasteur, 75724 Paris, France
*Correspondence: sigalb@ekmd.huji.ac.il
http://dx.doi.org/10.1016/j.devcel.2016.01.013

SUMMARY

Bacteria display an array of contact-dependent interaction systems that have evolved to facilitate direct cell-to-cell communication. We have previously identified a mode of bacterial communication mediated by nanotubes bridging neighboring cells. Here, we elucidate nanotube architecture, dynamics, and molecular components. Utilizing *Bacillus subtilis* as a model organism, we found that at low cell density, nanotubes exhibit remarkable complexity, existing as both intercellular tubes and extending tubes, with the latter frequently surrounding the cells in a "root-like" fashion. Observing nanotube formation in real time showed that these structures are formed in the course of minutes, displaying rapid movements. Utilizing a combination of super-resolution, light, and electron microscopy, we revealed that nanotubes are composed of chains of membranous segments harboring a continuous lumen. Furthermore, we discovered that a conserved calcineurin-like protein, YmdB, presents in nanotubes and is required for both nanotube production and intercellular molecular trade.

INTRODUCTION

Intercellular communication enables synergistic activity among bacterial community members, allowing the execution of complicated processes such as antibiotic production, secretion of virulence factors, and bioluminescence (Ng and Bassler, 2009). Conversely, intercellular communication may promote antagonistic effects, causing growth inhibition or lysis of neighboring cells, thus affording the perpetrator with a selective growth advantage (Hayes et al., 2010). Bacteria developed various elaborate apparatuses for establishing cell-to-cell contact, with the first mode to be discovered being conjugation, whereby genetic information is transferred from donor to recipient through a type IV secretion system fitted with flexible F pili (Lederberg and Tatum, 1946; Wang et al., 2009). Contact-mediated interactions can also be facilitated by the type III, V, and VI machineries, which allow exchange of cellular information among various species, as well as across kingdoms (Hayes et al., 2010). An additional mechanism underlying bacterial intercellular exchange involves shedding of membrane vesicles (MVs), which can fuse with both prokaryotic and eukaryotic cells. Importantly, the MV cargo is encased, and therefore protected from potentially harsh extracellular conditions (Schertzer and Whiteley, 2013). MVs, first identified decades ago, are features of both Gram-positive and -negative bacteria, and were found to harbor proteins, virulence factors, metabolites, signaling molecules, and even chromosomal DNA fragments (e.g., Mashburn and Whiteley, 2005; Matin and Konings, 1973; Rivera et al., 2010).

We have previously described a form of bacterial cell-to-cell interaction mediated by tubular protrusions, which we termed nanotubes, by analogy to their eukaryotic counterparts (Dubey and Ben-Yehuda, 2011). In eukaryotic cells, nanotubes facilitate intercellular transport of cytoplasmic molecules, membrane components, organelles, and even pathogens such as viruses (Abounit and Zurzolo, 2012). Utilizing *Bacillus subtilis*, we provided evidence that nanotubes serve as conduits for intercellular trade of cytoplasmic molecules and non-conjugative plasmids. Nanotubes were also formed in an interspecies manner, suggesting that they provide a route for trafficking constituents within and across species (Dubey and Ben-Yehuda, 2011). In support of this idea, cytoplasmic exchange of metabolites and proteins was reported to occur between different bacterial species and to be associated with nanotube-like structures (Benomar et al., 2015; Pande et al., 2015). Here we report that *B. subtilis* nanotubes are composed of constricted lipid bilayer segments, and identify YmdB as a component required for nanotube formation and intercellular molecular exchange.

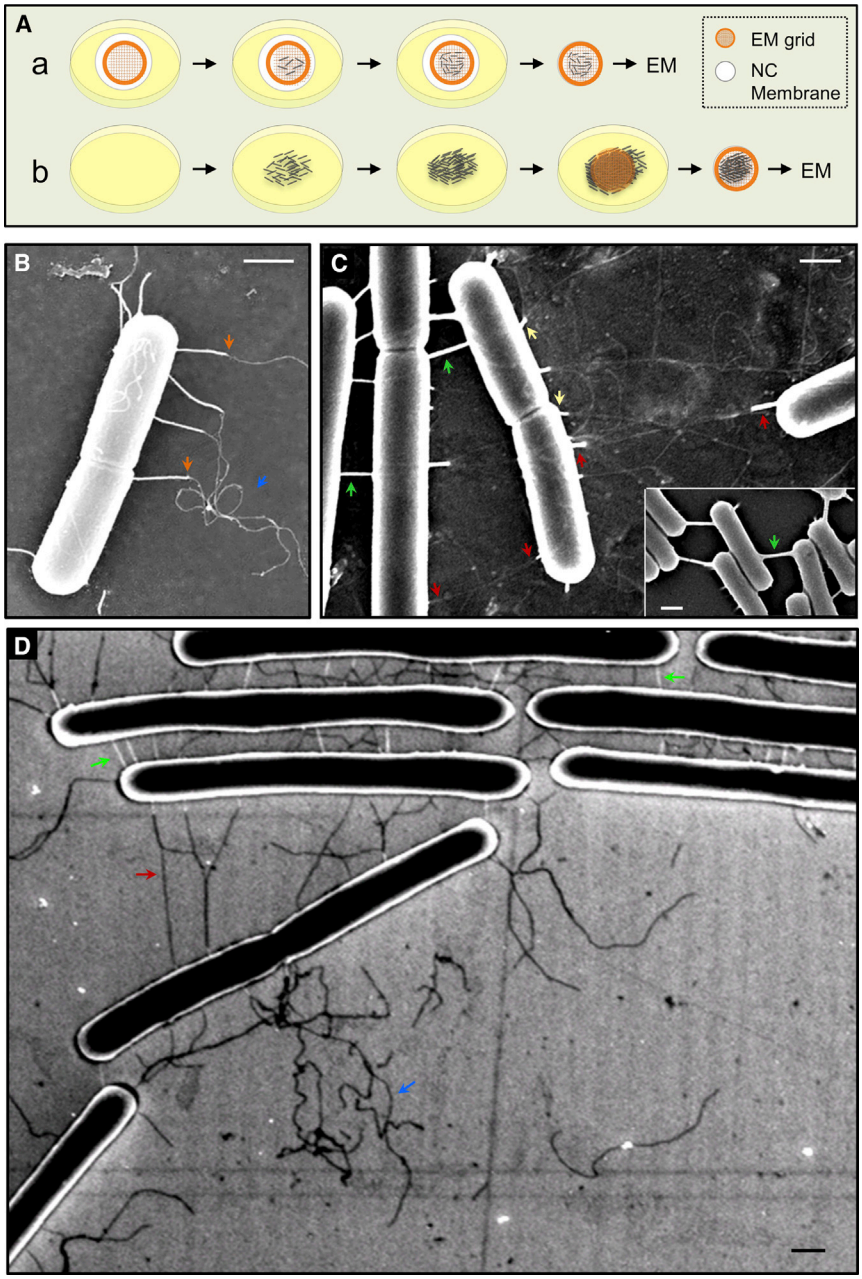

Figure 1. Extended Nanotubes Produced by Cells at Low Density

(A) Schematic representing the procedures utilized to observe nanotubes by EM. (a) Exponentially growing cells are spotted at low density onto an EM grid that is placed over a nitrocellulose (NC) membrane and incubated on solid LB for 2 hr. Grids are detached from the membrane and cells as well as their surroundings are observed by EM. (b) Cells are grown for 3 hr on solid LB at 37°C, and an EM grid is then placed over the cells. After 3 additional hours of incubation, cells attached to the grid are observed by EM.

(B and C) PY79 (wild-type) cells were spotted onto EM grids at low density and processed as depicted in (Aa). (B) HR-SEM image (×70,000) of a typical single cell surrounded by extending nanotubes. (C) HR-SEM image (×50,000) of extending and intercellular nanotubes. Inset shows typical short intercellular nanotubes formed at high cell density, visualized by HR-SEM (×40,000), as depicted in (Ab).

(D) PY79 cells were spotted at low density onto an ITO-coated coverslip and covered with a dialysis membrane. Cells were incubated at 37°C in LB medium for 2 hr, and subsequently fixed and visualized by HR-SEM (×6,000) without coating.

Green arrows: short intercellular nanotubes; red arrows: extending intercellular nanotubes; blue arrows: extending nanotube webs; yellow arrows: sites of extending nanotube emergence; orange arrows: nanotubes exhibiting both bright and dark appearance. Scale bars represent 500 nm.

See also Figure S1.

RESULTS

Elongated Nanotubes Extend from Cells Grown at Low Density

To investigate whether nanotube production is an intrinsic property of bacterial cells occurring regardless of the presence of neighbors, we examined nanotube formation by cells grown at low density. To observe single cells and their surrounding area, we devised a technique to grow bacteria on top of electron microscopy (EM) grids (Figure 1Aa), as opposed to our previous method whereby grids were placed over the growing bacteria (Figure 1Ab). Cells were spotted at low density onto an EM grid, incubated on solid Luria-Bertani (LB) medium for 2 hr, and visualized using high-resolution scanning EM (HR-SEM). During this time, the majority of cells were lacking proximal neighbors. Strikingly, we observed that single cells produce elongated tubular protrusions frequently arranged in a "root-like" fashion, extending over the surface to a distance of a few microns (Figure 1B). The outline of these projections was also evident by whole-mount transmission EM (Figure S1A). Such extensions were readily visible in a flagellum mutant (Figure S1B), ruling out the possibility that these appendages are flagella. We termed these elongated structures "extending nanotubes," as they extend away from the cell to distances of a few microns.

A closer observation of cells grown at low density indicated that extending nanotubes, encountering distal cells, could interconnect the two partners, likely turning into "long-distance" intercellular nanotubes (Figure 1C, red arrows). Noticeably, when cells were lying in proximity, we could often observe "short-distance" intercellular nanotubes (<1 μm), slightly above the surface, displaying manifestation comparable with the nanotubes produced at high cell density that we described previously (Figure 1C, inset and green arrows) (Dubey and Ben-Yehuda, 2011). When extending nanotubes originated from cells at a higher focal position, the site of emergence was brighter

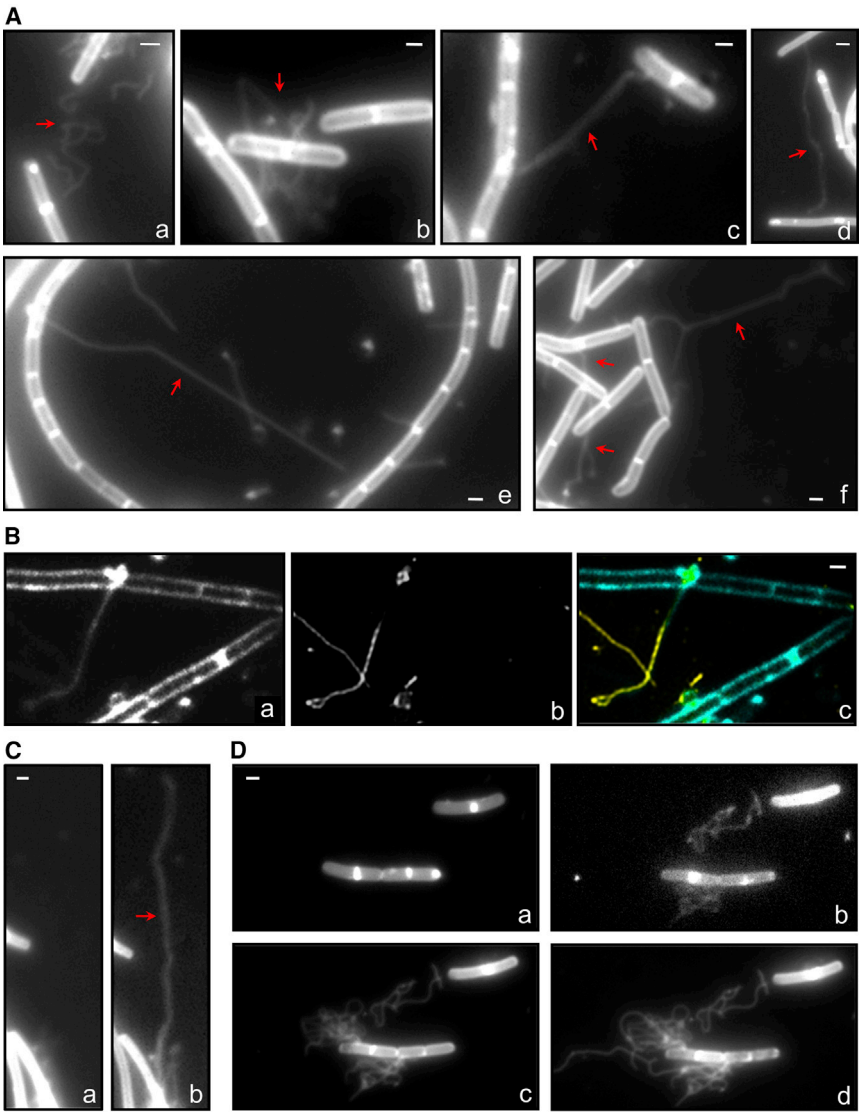

Figure 2. Live-Cell Imaging of Nanotube Formation and Dynamics

(A) GD215 (*Δhag*) cells were spotted at low density onto an ITO-coated coverslip and incubated in LB supplemented with a fluorescent membrane dye. Shown are fluorescence images showing webs of extending tubes (a, b) or elongated extending tubes (c–f). Nanotubes are highlighted by arrows. Cells are frequently off focus to improve nanotube visualization.

(B) GD215 cells were grown as in (A) and observed by TIRF-SIM. Shown are fluorescence of cells (a), TIRF-SIM of a nanotube (b), and an overlay of (a) (cyan) and (b) (yellow) images (c).

(C) GD215 cells were grown as in (A). Shown are fluorescence images captured at t = 0 (a) and t = 15 (b) min of incubation. Long-distance nanotube is highlighted by an arrow.

(D) GD215 cells were grown as in (A). Shown are fluorescence images captured at t = 0 (a), t = 30 (b), t = 50 (c), and t = 70 (d) min of incubation.

Cells photographed by LM are frequently off focus to improve nanotube visualization. Scale bars represent 500 nm.

See also Figure S1.

(Figure 1C, yellow arrows), similar in appearance to the short intercellular nanotubes. Furthermore, a single extending nanotube frequently exhibited both bright and dark regions that correlated with focal position (Figure 1B, orange arrows), implying that short intercellular and extending nanotubes are similar, and that only the focal position leads to their apparently dissimilar morphology.

To improve visualization, we developed a method to view nanotubular networks in uncoated samples by growing the cells over a coverslip (Figure S1C). In this technique the cells and nanotubes appear darker by HR-SEM imaging due to electrical charging. The absence of coating material exposed the complexity and prevalence of nanotubes, as well as the relatively uniform appearance of all nanotube types (Figure 1D). Cells lacking nearby neighbors produced elongated webs of extending tubes (Figure 1D, blue arrow), while cells with nearby neighbors developed elaborate intercellular networks. As before, extending nanotubes appeared to become intercellular upon reaching adjacent cells (Figure 1D, red arrow), whereas short nanotubes were evident when cells were residing close by (Figure 1D, green arrows).

Previously we provided evidence that nanotubes are sensitive to detergent treatment, indicative of a membranous composition (Dubey and Ben-Yehuda, 2011); therefore, we attempted to visualize nanotubes by light microscopy (LM) using a fluorescent membrane dye. When cells lacking flagella were grown at low density and stained with a membrane dye, complex ''root-like'' structures were frequently observed to surround the cells (Figures 2Aa and 2Ab), resembling the extending nanotubes observed by EM (e.g., Figure 1B). Furthermore, long-distance nanotubes, connecting cells located microns away, were manifested (Figures 2Ac–2Af). Of note, due to the fine structure of nanotubes, their visualization by membrane dye was enabled when cells were overexposed. Importantly, tracking the cells with SYTOX Green, which exclusively stains dead cells, indicated that nanotubes were formed by intact living cells (Figure S1D). The observed structures were not stained by fluorescently labeled wheat germ agglutinin, which recognizes peptidoglycan components, suggesting that nanotubes lack cell wall layers (Figure S1E). Frequently, nanotubes were observed in a focal plane different from that of the cells. To selectively observe nanotubes relative to background fluorescence, we combined total internal reflection fluorescence (TIRF) with super-resolution structured illumination microscopy (SIM). Indeed, the TIRF-SIM approach corroborated the existence of nanotubes located beneath the cells (Figures 2B and S1F). Notably, we could frequently detect extending nanotubes emanating from septal positions.

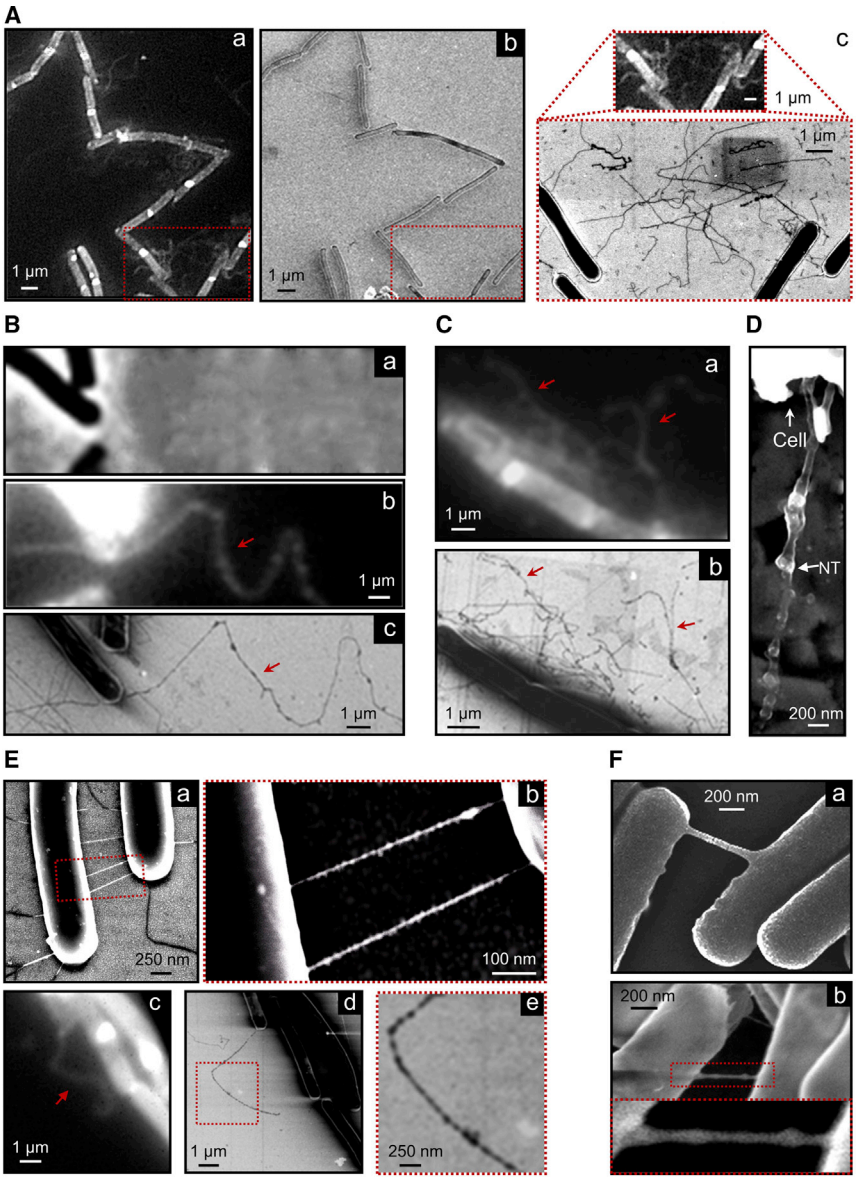

Figure 3. Visualization of Nanotubes Using cLM-SEM

(A) PY79 (wild-type) cells were spotted at low density onto an ITO-coated gold numbered coverslip and covered with a dialysis membrane. Cells were incubated in LB supplemented with a fluorescent membrane dye. At t = 40 min, when nanotubes were prominent, cells were fixed and visualized by HR-SEM without coating. Of note, some movement in cell and nanotube positions might occur before and during sample processing. Shown are fluorescence (before fixation) (a) and SEM (×1,250) (b) images. (c) A higher-magnification HR-SEM image (×10,000) of the boxed region shown in (a, b). For a direct comparison, the corresponding region, as captured by LM, is shown above.

(B) PY79 cells were processed as in (A). Shown are phase contrast (a), fluorescence (b), and HR-SEM (×12,500) without coating (c) images. Red arrow indicates the precise correlation of a single nanotube observed by both techniques.

(C) PY79 cells were processed as in (A). Shown are fluorescence (a) and HR-SEM (×17,500) without coating (b) images. Arrows indicate sites of precise correlation of nanotubes observed by both techniques.

(D) PY79 cells were spotted onto EM grids at low density and processed as depicted in Figure 1Aa. Shown is a nanotube emanating from a cell as visualized by HR-SEM (×100,000) without coating. A cell and a nanotube (NT) are indicated by arrows.

(E) PY79 cells were processed as in (A). (a) HR-SEM image (×50,000) without coating highlighting short intercellular nanotubes. (b) Higher-magnification HR-SEM image (×175,000) of the boxed region in (a). (c) Fluorescence image of a field of cells. Arrow indicates an extending nanotube. (d) HR-SEM image (×7,500) without coating of the field shown in (c). (e) Enlargement of the boxed region in (d).

(F) PY79 cells were spotted on solid LB and processed as depicted in Figure 1Ab. (a) HR-SEM image (×40,000) of cells coated with gold prior to visualization. A typical intercellular nanotube appears homogeneous. (b) HR-SEM image (×40,000) of non-coated cells. Insert shows enlargement of the boxed region in (b).

Cells photographed by LM are frequently off focus to improve nanotube visualization.

See also Figure S2.

To determine whether the membrane-stained tubular structures are indeed the nanotubes observed by EM, we developed a correlative LM and scanning EM (cLM-SEM) procedure (Figure S2A). Cells were spotted at low density onto a conductive gold numbered coverslip and tracked by time-lapse microscopy until the extracellular structures were prominent (Figure 3Aa). Subsequently, cells were fixed and the corresponding region viewed by scanning EM (Figure 3Ab). Our analysis revealed a substantial correlation between the tubular extensions observed by LM and scanning EM (Figure 3Ac). Furthermore, examining either single extended tubes or complex "root-like" patterns confirmed that the structures monitored by both methods are identical (Figures 3B and 3C). Thus, we conclude that nanotubes exist in short intercellular and extending modes, with the latter being prominent at low cell density.

Real-Time Imaging of Nanotube Formation and Dynamics

Next, we followed nanotube formation and kinetics in real time within a low-density population, prior to growth resumption, when cells were presumably in lag phase. Remarkably, we observed that a single nanotube could extend to a distance of approximately 15 μm within 15 min (Figure 2C). As anticipated, we could sometimes capture an intermediate stage at which an extending nanotube turned intercellular (Figure S2B). Analysis of a field of cells initially lacking visible nanotubes (Figure 2Da) revealed the generation of a network of extending tubes 30 min post incubation (Figure 2Db) that reached an estimated overall length of 40 μm after 50 min (Figures 2Dc and S2C). Eventually, after 70 min, nanotube growth attained an approximate length of 57 μm with a corresponding surface

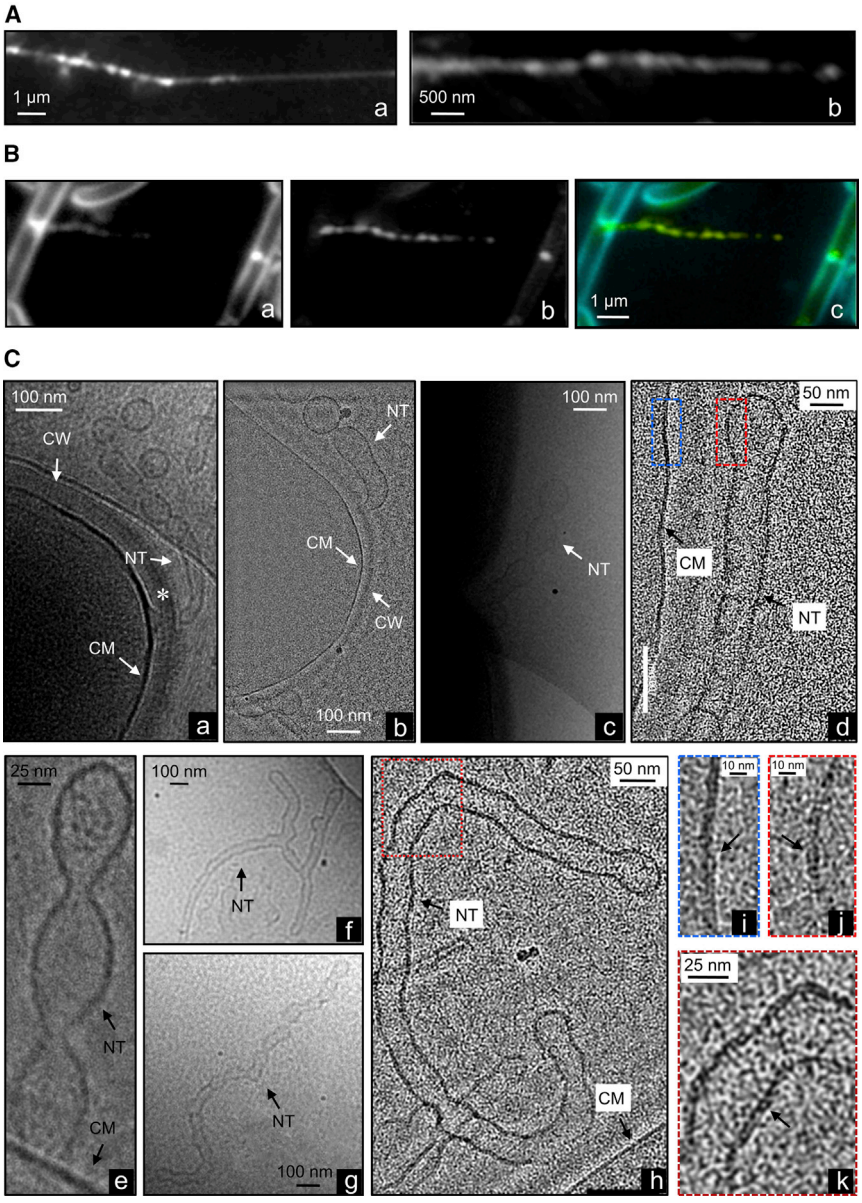

Figure 4. Nanotubes Exhibit Architecture of Consecutive Constricted Segments

(A) GD215 (*Δhag*) cells were spotted at low density onto an ITO-coated coverslip and incubated in LB supplemented with a fluorescent membrane dye. Shown are examples of typical nanotubes observed by fluorescence (a) and TIRF-SIM (b).

(B) GD215 cells were grown as in (A) and observed by TIRF-SIM. Shown are epi-fluorescence of cells (a), TIRF-SIM of a nanotube (b), and an overlay of (a) (cyan) and (b) (yellow) images (c).

(C) GB168 (*Δhag*, *ΔymdB*, $P_{hyper\text{-}spank}$-*ymdB*) cells, having higher level of nanotubes due to YmdB overexpression, were incubated at 37°C in LB for 2 hr, vitrified and visualized by cryo-EM. (a) Image (×42,000) of a nanotube emanating from a cell. Asterisk indicates the tube emanation site. (b) Image (×42,000) of a nanotube emanating from a cell. (c) Image (×42,000) of a nanotube that seems to emanate from the division septum. (d) Image (×42,000) of a nanotube located along the cell. Nanotube circumference and cell membrane appear identical. (e) Image (×64,000) of a nanotube emanating from the cell and having a constricted pattern. (f–h) Examples of extending nanotubes (f and g, ×8,700; h, ×42,000), detached from the cells, having a continuous lumen. (i, j) Enlarged view of the boxed regions in (d). Nanotube membrane bilayer is indicated by arrows. (k) Enlarged view of the boxed region in (h). Nanotube tube membrane bilayer is indicated by an arrow. NT, nanotube; CM, cell membrane, CW, cell wall.

See also Figure S2.

area of 9 μm^2 (Figures 2Dd and S2C), which is almost three times larger than the calculated surface of a typical *B. subtilis* cell (3.14 μm^2; Figure S2C). This tremendous increase in cell surface area raises the possibility that nanotubes serve to scavenge for nutrients. Indeed, following nanotube motion over a period of a few minutes revealed rapid nanotube movements, on a timescale of milliseconds (Movies S1 and S2), supporting the premise that nanotubes could serve to explore the surroundings. Whether this motion is energy dependent or Brownian is currently under investigation.

We then sought to monitor the presence of cytoplasmic cargo within tubes by exploiting the small fluorophore calcein acetoxymethylester (AM) (623 Da), which becomes caged within the cytoplasm and was found to be rapidly exchanged among neighbors (Dubey and Ben-Yehuda, 2011). Signal from calcein was readily detected from areas surrounding the cells in structures corresponding to nanotubes (Figure S2D). Frequently, the extracellular calcein signal appeared punctate (Figure S2Da), a pattern likely reflecting the nanotube structure as further explored below.

Nanotubes Comprise Consecutive Constricted Membranous Segments

A detailed examination of nanotubes in non-coated HR-SEM specimens revealed both short and extending tubes to apparently be composed of chains of sequential beads (Figures 3D–3F). By advancing our method to a triple correlative LM-SEM-atomic force microscopy (AFM) procedure (Figure S2A), we corroborated that nanotubes observed by scanning EM are segmented (Figure S2E and S2F). Similar nanotube beaded patterns were visible in living cells using fluorescence microscopy (Figure 4Aa), and more clearly by TIRF-SIM imaging (Figures 4Ab and 4B).

We next aimed to explore whether nanotube segments have a shared lumen or whether each corresponds to a separate compartment by analyzing the ultrastructural details of nanotubes using cryo-EM in close to native conditions. Utilizing this approach we were able to image nanotubes that directly emanate from the cell membrane, crossing the cell wall through a narrow orifice, and extending into the surrounding area (Figures 4Ca–4Ce). Frequently we observed nanotubes that were

detached from nearby cells (Figures 4Cf–4Ch). Typically, nanotubes appeared as a chain of consecutive constricted segments having a continuous lumen (Figures 4Cc–4Ch). Sometimes these constrictions were less evident and the tubes appeared more homogeneous in width (Figures 4Cd and 4Cf–4Ch), while in other cases the constriction sites were prominent and free vesicles seemed to be released from the nanotubes (Figures 4Ca and 4Cb). Ultra-resolution analysis further disclosed that nanotubes are encased by a membrane that appears identical to the cytoplasmic membrane, containing the characteristic lipid bilayer and devoid of a noticeable cell wall (Figures 4Cd and 4Ch–4Ck).

Cryo-EM analysis indicated the nanotube width to be approximately 40–60 nm. Consistently, estimations based on non-coated high-magnification HR-SEM samples ($\geq \times 100{,}000$) showed the tube width to range from 50 to 70 nm (data not shown). These measurements fall within the range of our previous estimations based on gold-coated samples (30–120 nm; Dubey and Ben-Yehuda, 2011). As judged by cryo-EM, at constricted sites nanotube width was reduced to ~20 nm, while the length of individual nanotube segments, as defined by two constriction sites, was ~100 nm.

YmdB Is Required for Nanotube Formation and Intercellular Molecular Trade

To elucidate the molecular components comprising nanotubes, we devised a procedure to enrich for nanotubes deriving from growing cells (Figure S3A) and to dissect their proteinaceous composition by mass spectrometry (MS). Using this strategy, 52 proteins, mainly involved in basic metabolism, cell wall remodeling, or lacking a known function, were enriched in the nanotube fraction (Table S1). An intriguing protein identified was TasA, previously shown to generate extracellular amyloidic fibers crucial for biofilm integrity (Branda et al., 2006; Stover and Driks, 1999). However, HR-SEM and AFM analyses revealed that nanotubes are produced by *tasA* mutant cells (Figures S3B and S3C), indicating that TasA is not essential for tube formation. Notably, no additional biofilm matrix components were detected in the nanotube fraction.

Next, we investigated the impact of the potential nanotube-associated proteins on intercellular molecular exchange. Previously we found that mixing two strains, each harboring a different antibiotic resistance gene, results in the exchange of cytoplasmic molecules potentially through nanotubes, yielding a population of cells temporarily resistant to both antibiotics. Furthermore, we detected the delivery of a non-conjugative plasmid from donor to recipient, in a mode independent of natural transformation (Figure S3E) (Dubey and Ben-Yehuda, 2011). We next exploited these antibiotic assays as screens to assess nanotube functionality in strains deleted for the potential nanotube-associated genes. We identified several mutants exhibiting attenuated molecular exchange, with Δ*ymdB* showing the most severe deficiency (Figure S3D). YmdB is a phosphodiesterase that was reported to function by decreasing the expression of motility genes and inducing genes implicated in biofilm formation (Diethmaier et al., 2011, 2014). However, examining the capacity of *tasA*, as well as an array of biofilm mutant strains, to exchange molecules, did not reveal significant impairment (Figures S3F–S3H and Table S2), suggesting that these proteins are not required for nanotube functionality.

A detailed examination revealed that both protein and plasmid trading were significantly decreased in *ΔymdB* cells, a deficiency that was most evident at low cell density (Figures 5Aa, 5Ad, S4Aa, and S4Ad). Furthermore, this phenotype was prominent when only the donor strain harbored the *ymdB* mutation (Figures 5Ab and S4Ab). Conversely, wild-type levels of molecular exchange were observed when only the recipient strain carried the *ymdB* mutation (Figures 5Ac and S4Ac). Thus, molecular trade of proteins and plasmids has a donor to recipient directionality that is largely dependent on production of YmdB by the donor. Interestingly, mutating a single residue within the conserved YmdB metal binding active site (Shin et al., 2008) resulted in a deficiency in molecular exchange similarly to *ΔymdB* cells (Figure S4B), indicating that YmdB enzymatic activity is required for the process. Finally, to substantiate the involvement of YmdB in intercellular molecular exchange, we employed the *cre/loxP* recombination system (Marx and Lidstrom, 2002), in which the donor strain contains a chromosomally integrated *cre* gene while the recipient harbors a cassette containing antibiotic resistance genes (Figure S4C). When *ΔymdB* strains were employed for this assay, the frequency of resistant colonies was reduced by approximately 25-fold (Figures S4D and S4E).

To decipher whether the decrease in molecular exchange of *ΔymdB* is a consequence of fewer nanotubes, we examined nanotube production by the mutant. At low cell density, we could hardly detect nanotubes deriving from the mutant cells (Figure 5Ba), and consistently their occurrence was reduced when cells were grouped together (Figure S4Fa). This phenotype was complemented by the ectopic insertion of the *ymdB* gene (Figures 5Bb and S4Fb). Estimating the number of nanotube-producing cells using EM revealed that 95% of the wild-type cells harbored nanotubes, whereas less than 5% of *ΔymdB* cells displayed such structures. Since *ΔymdB* cells could serve as recipients for molecular exchange, we investigated whether nanotubes can be formed between wild-type and *ΔymdB* cells. When *ΔymdB* strain, harboring cytoplasmic GFP, was grown in a mixture with *ymdB* strain and subjected to cLM-SEM, GFP producers lacked visible nanotubes (Figures 5C, S4G, and S4H, green arrows), whereas tube generation by *ymdB*-expressing cells was evident (Figures 5C, S4G, and S4H, red arrows). However, when lying in proximity, nanotubes connecting *ymdB* and *ΔymdB* cells were manifested (Figures 5C and S4H, orange arrows), reinforcing the view that the mutant cells can act as recipients for molecular exchange.

YmdB Localizes to the Cytoplasm, Cell Periphery, and Nanotubes

To gain insight into YmdB mode of operation, we examined its subcellular localization. A strain harboring a functional *ymdB-gfp* fusion as the sole chromosomal copy exhibited a relatively weak fluorescence signal that seems diffuse or punctate within the cell (Figure S5A). Consequently, we employed the super-resolution technique photoactivated localization microscopy (PALM) that enables localization of single protein molecules with resolution down to ~20 nm (Betzig et al., 2006). Fusing YmdB to the photoactivatable fluorescent protein PA-mCherry (Subach et al., 2009) revealed YmdB-PA-mCherry to preferentially locate to the cell circumference, often concentrated in foci-like assemblies (Figures 5DAa, 5Dc, and S5B) in a frequency

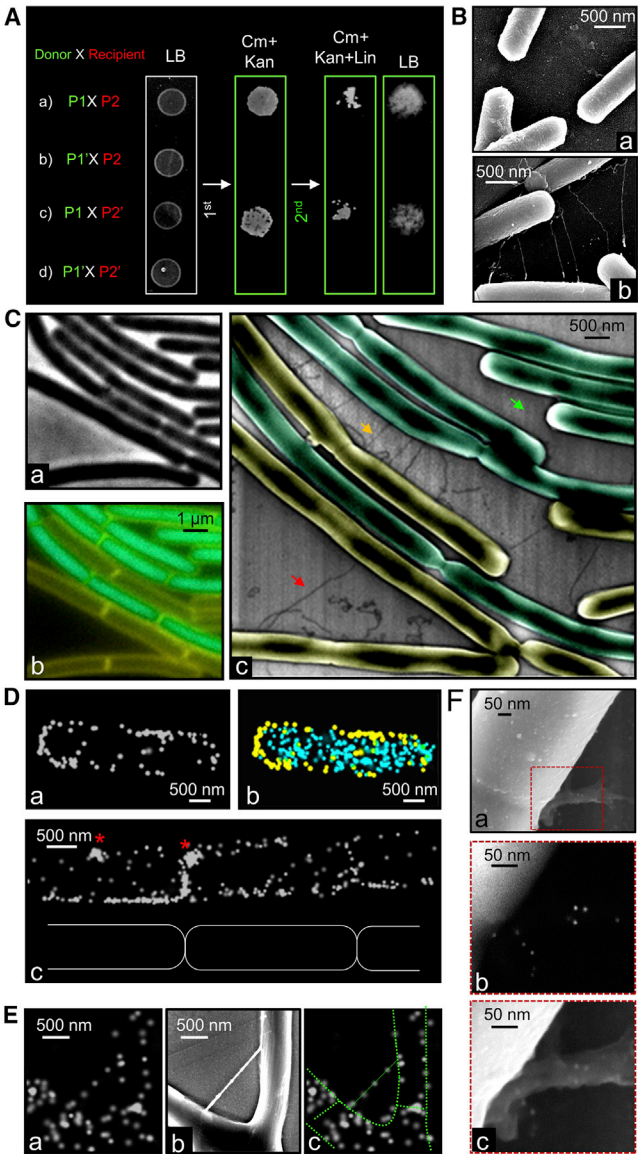

Figure 5. *ymdB* Is Required for Nanotube Formation and Molecular Exchange

(A) Examination of molecular exchange in *ymdB* mutant strains. The strains used are: P1 (GD110: *amyE*::$P_{hyper\text{-}spank}$-*cat-spec*, pHB201/*cat*, *erm*) (Cm^R, $Spec^R$, MIs^R), P2 (SB513: *amyE*::$P_{hyper\text{-}spank}$-*gfp-kan*) (Kan^R), P1′ (GB69) and P2′ (GB77) strains have the corresponding genotypes and harbor the *ΔymdB*::*tet* allele. Strains were mixed in a 1:1 ratio (OD_{600} 0.1) at the indicated combinations (a–d), spotted on LB + isopropyl β-D-1-thiogalactopyranoside plates, grown for 4 hr at 37°C, replica plated onto Cm + Kan antibiotic plates (first replica plating, protein transfer), and incubated overnight at 37°C. Next, cells grown on Cm + Kan antibiotic plates were re-replica plated onto Cm + Kan + Lin antibiotic plates (second replica plating, plasmid transfer), and incubated overnight at 37°C. Donor and recipient strains are highlighted in green and red, respectively. Part of Figure S4A.

(B) Shown are gold-coated HR-SEM images of GB61 (*ΔymdB*) (×80,000) (a) and GB115 (*ΔymdB*, *amyE*::$P_{hyper\text{-}spank}$-*ymdB*) (×100,000) (b). Cells were spotted onto EM grids at low density and processed as depicted in Figure 1Aa.

(C) GB168 (*ΔymdB, Δhag, amyE*::$P_{hyper\text{-}spank}$-*ymdB*) and GB121 (*ΔymdB, Δhag, amyE*::P_{rrnE}-*gfp*) cells were mixed and spotted at low density onto an ITO-coated gold numbered coverslip. Cells were incubated in LB medium supplemented with a fluorescent membrane dye. At t = 1 hr, cells were visualized by LM, fixed, and observed by HR-SEM without coating. Shown are phase (a), fluorescence (cyan, GFP; yellow, membrane staining) (b), and HR-SEM (×20,000) (c) images of a field of cells. Cells were pseudo-colored cyan (*ymdB* mutant) and yellow (*ymdB* producer) according to (b). Red arrow: intercellular nanotubes surrounding wild-type cells; green arrow: no visible intercellular nanotubes surrounding *ΔymdB* cells; orange arrow: visible intercellular nanotubes between wild-type and *ΔymdB* cells. Scale bars represent 500 nm.

(D) GB195 (*Δhag, ymdB-PA-mCherry*, *rplA-dronpa*) cells were grown at 37°C in LB and visualized by PALM. (a) Localization of YmdB-PA-mCherry molecules in a single cell. (b) Localization of both YmdB-PA-mCherry (yellow) and RplA-Dronpa (cyan) molecules in the cell shown in (a). (c) Localization of YmdB-PA-mCherry molecules in a chain of cells, as illustrated below. Asterisks indicate clusters of YmdB molecules.

(E) GB195 (*Δhag, ymdB-PA-mCherry, rplA-dronpa*) cells were spotted at low density onto an ITO-coated gold numbered coverslip, incubated in LB for 1 hr, fixed, and visualized by PALM and HR-SEM without coating. Shown are PALM image of YmdB-PA-mCherry molecules from cells (a), a corresponding HR-SEM image (×65,000) (b), and an illustration of the cells and nanotube outlines over PALM image (green dotted lines) (c).

(F) GB117 (*ΔymdB*, *amyE*::$P_{hyper\text{-}spank}$-*ymdB-gfp*) cells were spotted onto EM grids at low density and processed as depicted in Figure 1Aa. Cells were subjected to immuno-gold scanning EM using primary antibodies against GFP and secondary gold-conjugated antibodies. Samples were not coated before observation. White dots indicate the localization of YmdB molecules. Shown are HR-SEM images (×350,000) acquired using TLD-SE (a), and an enlargement of the boxed region in (a) acquired using vCD (low-kV high-contrast detector) (b) and TLD-SE (c) modes.

See also Figures S3–S5.

of approximately one per cell. A similar localization pattern was seen when YmdB was fused to Dronpa (Ando et al., 2004) (Figure S5C). Using PALM in two colors (Sherman et al., 2011), we generated a fusion of Dronpa with the ribosomal subunit RplA; in this case the fusion protein clearly filled the cytoplasmic space (Figures 5Db and S5Bb). Consistent with these findings, biochemical fractionation revealed YmdB to be in the cytoplasmic fraction and to associate with the membrane (Figures S5D and S5E).

Western blot analysis detected an abundance of YmdB in the nanotube fraction, corroborating the MS data (Figures S5D and S5E). To demonstrate the direct localization of YmdB to nanotubes, we developed a correlative PALM-scanning EM (cPALM-SEM) procedure, aimed at localizing single YmdB molecules over nanotubes. Indeed, we observed YmdB molecules that clearly coincided with nanotubes (Figure 5E). In parallel, immuno-HR-SEM analysis showed that YmdB-GFP molecules specifically co-localize with nanotubes (Figures 5F and S5F). Collectively, the evidence uncovers that YmdB is associated with the cell periphery and nanotubes.

DISCUSSION

We propose that nanotube networks are key elements in the bacterial capacity to sense, respond, explore the surroundings, and communicate with their neighbors. When lacking nearby neighbors, cells produce extensive elongated nanotubes that greatly increase the cell surface area. Such nanotube networks may serve to facilitate delivery of distant nutrients and establish a conduit between remote cells, while short intercellular nanotubes appear to prevail among adjacent cells. Cryo-EM analysis evidences that nanotubes emerge from the cytoplasmic

membrane and cross the thick cell wall layers. We speculate that peptidoglycan-modifying enzymes trigger nanotube formation by locally tearing the cell wall. Indeed, several cell wall remodeling enzymes, such as amidases and penicillin-binding proteins, were enriched in the nanotube fraction (Table S1). Nanotubes could also utilize this arsenal of enzymes to pave their way and fuse with neighboring cells. Each nanotube segment may reflect a single membrane-budding event, with frequent occurrence of such events promoting nanotube elongation. Nanotubes could further elongate and even bud to yield free MVs. Environmental and physiological conditions may affect the balance between nanotube elongation and MV release.

Recently, the ability of distant bacterial species to exchange cytoplasmic molecules such as nutrients, metabolites, and proteins has been demonstrated to take place under starvation between *Acinetobacter baylyi* and *Escherichia coli*, as well as between Gram-positive and -negative anaerobes. This cross-feeding phenomenon occurs in a contact-dependent fashion and relies on the formation of nanotubular structures, implying that nanotube-associated molecular exchange is prominent in nature (Benomar et al., 2015; Pande et al., 2015). Additional membranous extracellular structures were found to serve for intercellular molecular trade as well as for other physiological properties. For example, studies in *Myxococcus xanthus* indicate the existence of intercellular outer MV chains, encompassing outer membrane proteins known to be exchanged among cells (e.g., Ducret et al., 2013; Remis et al., 2014; Wei et al., 2014). The Gram-negative *Delftia*, on the other hand, produces MV chains termed nanopods in response to a unique carbon source, suggesting that nanopods are involved in nutrient uptake (Shetty et al., 2011). Furthermore, nanowires in *Shewanella oneidensis* MR-1, utilized for electron transport, were shown to be composed of outer membrane and periplasmic extensions (Pirbadian et al., 2014).

The finding that YmdB plays a key role in nanotube formation and subsequently in molecular exchange raises the question of how this protein operates. Crystal structure and enzymatic analysis of YmdB revealed that it harbors a metallophosphodiesterase conserved domain, required to hydrolyze cyclic nucleotides such as cyclic AMP (cAMP) (Diethmaier et al., 2011, 2014). Notably, cAMP and cyclic diguanosine monophosphate have been implicated in controlling social activities in microbes by acting as secondary messengers (e.g., Boyd and O'Toole, 2012; Hengge, 2009). Furthermore, we have recently found that YmdB is required for proper colony development in a manner that is dependent on cellular cAMP levels (Mamou et al., 2016). Hence, we speculate that YmdB, which localizes to the cell periphery, senses and hydrolyzes cAMP from external sources, thereby transmitting a message to produce nanotubes. Furthermore, YmdB localization to nanotubes could serve to sense neighbors and navigate tube growth toward the detected stimulus. Such an external signal may also modulate YmdB subcellular localization, creating high local concentrations of protein molecules, as observed by PALM, that subsequently recruit additional nanotube machinery components. A recent study described an overall effect of *ymdB* on mRNA levels of many genes, including those involved in motility, biofilm formation, and sugar utilization (Diethmaier et al., 2014). We suggest that this global effect could be due to a YmdB sensory function that affects cell physiology. YmdB is highly conserved among Gram-positive and -negative bacteria, implying that it plays a fundamental role in bacterial physiology in nature.

EXPERIMENTAL PROCEDURES

Bacterial Strains and General Methods

Plasmids, *B. subtilis* strains, primers, and general methods are described in Supplemental Experimental Procedures.

Fluorescence Microscopy

For observing nanotube development in real time, exponentially growing cells were spotted at low density onto an indium tin oxide (ITO)-coated coverslip (see Supplemental Experimental Procedures) and covered with a dialysis membrane. The coverslip was then assembled into a mounting frame (A-7816, Invitrogen) filled with liquid LB supplemented with 1 μg/ml FM4-64 fluorescent membrane dye (Invitrogen), when indicated. Cells were incubated in a temperature-controlled chamber at 37°C and tracked by LM. For time-course visualization of nanotubes, cells were grown at low density at 37°C with gentle shaking (25 rpm). Samples were removed during mid-logarithmic phase, pelleted gently (2,000 rpm), spread onto a poly-lysine-coated coverslips, and imaged by LM. Cells were visualized by Axio Observer Z1 (Zeiss), equipped with a CoolSnap HQII camera (Roper Scientific). System control and image processing were performed with MetaMorph 7.7.5 software (Molecular Devices).

For TIRF-SIM visualization, cells were incubated as described above. Images were acquired using a Nikon nSIM microscope equipped with a TIRF module in 2D mode. For each super-resolution image, nine images were taken and examined for presence of grid pattern. The final image was reconstructed using NIS-Elements software (Nikon).

cLM-SEM-AFM

The procedure for cLM-SEM-AFM visualization is depicted in Figure S2A. Cells were spotted onto a gold numbered ITO-coated coverslips and processed as described for observing nanotube development in real time (see above). Gold numbers allowed locating the coordinates of a given region in all three microscopy procedures. When nanotubes were prominent by LM, liquid medium was removed and the coverslip was washed twice with PBSx1. Cells were then fixed with 2% glutaraldehyde in sodium cacodylate buffer (0.1 M, pH 7.2) for 2 hr at 25°C. Next, the dialysis membrane (molecular weight 12–14 kDa) was gently removed and cells, attached to coverslips, were washed twice with sodium cacodylate buffer. Coverslips were further processed as described in the standard scanning EM analysis (see Supplemental Experimental Procedures). Specimens were imaged without coating using a Through-Lens Detector operated at Secondary Electron (TLD-SE) mode by a Magellan XHR scanning electron microscope (FEI). AFM imaging and measurements were carried out using D3100 Nanoscope V multimode scanning probe microscope (Bruker). Images were recorded at ambient conditions using the tapping mode with single FESP silicon probe tip, having a resolution limit of less than 10 nm, a typical spring constant of about 3 N/m, and a resonance frequency around 75 kHz. Tapping force was controlled by the ratio between set point amplitude (A_{sp}) and free-air amplitude (A_0).

Additional procedures are described in Supplemental Experimental Procedures.

SUPPLEMENTAL INFORMATION

Supplemental Information includes Supplemental Experimental Procedures, five figures, two tables, and two movies and can be found with this article online at http://dx.doi.org/10.1016/j.devcel.2016.01.013.

AUTHOR CONTRIBUTIONS

Conceptualization, G.P.D., G.B.M.M., and S.B.-Y; Methodology, G.P.D., G.B.M.M., A.D., T.A., S.T., A. Rouvinski, D.K., E.S., O.M., and S.B.-Y.; Investigation, G.P.D., G.B.M.M., A.D., T.A., S.T., and S.B.-Y; Writing – Original Draft,

G.P.D., G.B.M.M., and S.B.-Y; Writing – Review & Editing, G.P.D., G.B.M.M., T.A., A. Rouvinski, D.K., O.M., and S.B.-Y; Resources, A. Rosenberg.

ACKNOWLEDGMENTS

We are grateful to I. Popov, E. Blayvas, A. Radko, S. Eliav, G. Chechelnitsky, M. Saidian, V. Gutkin (NanoCentre, Hebrew University), and the Center for Microscopy and Image Analysis, (Zurich University) for technical support. We are indebted to members of the Ben-Yehuda laboratory, G. Bachrach, I. Rosenshine, A. Taraboulos and J. Thrissur (Hebrew University), A.K. Tiwari (IISER), and B. Rosenberg (MIT) for help and valuable discussions. This work is supported by the ERC-Advance Grant (339984) and the Israel Science Foundation (ISF) (327/11) awarded to S.B.-Y., the Marie Skłodowska-Curie actions of the European Commission (321993) and the ISF (1937/13) awarded to E.S., the ERC-Starting Grant (337713) and ISF (843/11) awarded to D.K., and the Maexi foundation support to O.M. G.B.M.M. was supported by PBC-outstanding postdoctoral fellowship, Council for Higher Education, Israel.

Received: January 19, 2015
Revised: September 28, 2015
Accepted: January 22, 2016
Published: February 22, 2016

REFERENCES

Abounit, S., and Zurzolo, C. (2012). Wiring through tunneling nanotubes from electrical signals to organelle transfer. J. Cell Sci. *125*, 1089–1098.

Ando, R., Mizuno, H., and Miyawaki, A. (2004). Regulated fast nucleocytoplasmic shuttling observed by reversible protein highlighting. Science *306*, 1370–1373.

Benomar, S., Ranava, D., Cardenas, M.L., Trably, E., Rafrafi, Y., Ducret, A., Hamelin, J., Lojou, E., Steyer, J.P., and Giudici-Orticoni, M.T. (2015). Nutritional stress induces exchange of cell material and energetic coupling between bacterial species. Nat. Commun. *6*, 6283.

Betzig, E., Patterson, G.H., Sougrat, R., Lindwasser, O.W., Olenych, S., Bonifacino, J.S., Davidson, M.W., Lippincott-Schwartz, J., and Hess, H.F. (2006). Imaging intracellular fluorescent proteins at nanometer resolution. Science *313*, 1642–1645.

Boyd, C.D., and O'Toole, G.A. (2012). Second messenger regulation of biofilm formation: breakthroughs in understanding c-di-GMP effector systems. Annu. Rev. Cell Dev. Biol. *28*, 439–462.

Branda, S.S., Chu, F., Kearns, D.B., Losick, R., and Kolter, R. (2006). A major protein component of the *Bacillus subtilis* biofilm matrix. Mol. Microbiol. *59*, 1229–1238.

Diethmaier, C., Pietack, N., Gunka, K., Wrede, C., Lehnik-Habrink, M., Herzberg, C., Hubner, S., and Stulke, J. (2011). A novel factor controlling bistability in *Bacillus subtilis*: the YmdB protein affects flagellin expression and biofilm formation. J. Bacteriol. *193*, 5997–6007.

Diethmaier, C., Newman, J.A., Kovacs, A.T., Kaever, V., Herzberg, C., Rodrigues, C., Boonstra, M., Kuipers, O.P., Lewis, R.J., and Stulke, J. (2014). The YmdB phosphodiesterase is a global regulator of late adaptive responses in *Bacillus subtilis*. J. Bacteriol. *196*, 265–275.

Dubey, G.P., and Ben-Yehuda, S. (2011). Intercellular nanotubes mediate bacterial communication. Cell *144*, 590–600.

Ducret, A., Fleuchot, B., Bergam, P., and Mignot, T. (2013). Direct live imaging of cell-cell protein transfer by transient outer membrane fusion in *Myxococcus xanthus*. Elife *2*, e00868.

Hayes, C.S., Aoki, S.K., and Low, D.A. (2010). Bacterial contact-dependent delivery systems. Annu. Rev. Genet. *44*, 71–90.

Hengge, R. (2009). Principles of c-di-GMP signalling in bacteria. Nat. Rev. Microbiol. *7*, 263–273.

Lederberg, J., and Tatum, E.L. (1946). Gene recombination in *Escherichia coli*. Nature *158*, 558.

Mamou, G., Malli Mohan, G., Rouvinski, A., Rosenberg, A., and Ben-Yehuda, S. (2016). Early developmental program shapes colony morphology in bacteria. Cell Rep. Published online February 18, 2016. http://dx.doi.org/10.1016/j.celrep.2016.01.071.

Marx, C.J., and Lidstrom, M.E. (2002). Broad-host-range cre-lox system for antibiotic marker recycling in gram-negative bacteria. Biotechniques *33*, 1062–1067.

Mashburn, L.M., and Whiteley, M. (2005). Membrane vesicles traffic signals and facilitate group activities in a prokaryote. Nature *437*, 422–425.

Matin, A., and Konings, W.N. (1973). Transport of lactate and succinate by membrane vesicles of *Escherichia coli*, *Bacillus subtilis* and a *Pseudomonas* species. Eur. J. Biochem. *34*, 58–67.

Ng, W.L., and Bassler, B.L. (2009). Bacterial quorum-sensing network architectures. Annu. Rev. Genet. *43*, 197–222.

Pande, S., Shitut, S., Freund, L., Westermann, M., Bertels, F., Colesie, C., Bischofs, I.B., and Kost, C. (2015). Metabolic cross-feeding via intercellular nanotubes among bacteria. Nat. Commun. *6*, 6238.

Pirbadian, S., Barchinger, S.E., Leung, K.M., Byun, H.S., Jangir, Y., Bouhenni, R.A., Reed, S.B., Romine, M.F., Saffarini, D.A., Shi, L., et al. (2014). Shewanella oneidensis MR-1 nanowires are outer membrane and periplasmic extensions of the extracellular electron transport components. Proc. Natl. Acad. Sci. USA *111*, 12883–12888.

Remis, J.P., Wei, D., Gorur, A., Zemla, M., Haraga, J., Allen, S., Witkowska, H.E., Costerton, J.W., Berleman, J.E., and Auer, M. (2014). Bacterial social networks: structure and composition of *Myxococcus xanthus* outer membrane vesicle chains. Environ. Microbiol. *16*, 598–610.

Rivera, J., Cordero, R.J., Nakouzi, A.S., Frases, S., Nicola, A., and Casadevall, A. (2010). *Bacillus anthracis* produces membrane-derived vesicles containing biologically active toxins. Proc. Natl. Acad. Sci. USA *107*, 19002–19007.

Schertzer, J.W., and Whiteley, M. (2013). Bacterial outer membrane vesicles in trafficking, communication and the host-pathogen interaction. J. Mol. Microbiol. Biotechnol. *23*, 118–130.

Sherman, E., Barr, V., Manley, S., Patterson, G., Balagopalan, L., Akpan, I., Regan, C.K., Merrill, R.K., Sommers, C.L., Lippincott-Schwartz, J., et al. (2011). Functional nanoscale organization of signaling molecules downstream of the T cell antigen receptor. Immunity *35*, 705–720.

Shetty, A., Chen, S., Tocheva, E.I., Jensen, G.J., and Hickey, W.J. (2011). Nanopods: a new bacterial structure and mechanism for deployment of outer membrane vesicles. PLoS One *6*, e20725.

Shin, D.H., Proudfoot, M., Lim, H.J., Choi, I.K., Yokota, H., Yakunin, A.F., Kim, R., and Kim, S.H. (2008). Structural and enzymatic characterization of DR1281: a calcineurin-like phosphoesterase from *Deinococcus radiodurans*. Proteins *70*, 1000–1009.

Stover, A.G., and Driks, A. (1999). Secretion, localization, and antibacterial activity of TasA, a *Bacillus subtilis* spore-associated protein. J. Bacteriol. *181*, 1664–1672.

Subach, F.V., Patterson, G.H., Manley, S., Gillette, J.M., Lippincott-Schwartz, J., and Verkhusha, V.V. (2009). Photoactivatable mCherry for high-resolution two-color fluorescence microscopy. Nat. Methods *6*, 153–159.

Wang, Y.A., Yu, X., Silverman, P.M., Harris, R.L., and Egelman, E.H. (2009). The structure of F-pili. J. Mol. Biol. *385*, 22–29.

Wei, X., Vassallo, C.N., Pathak, D.T., and Wall, D. (2014). Myxobacteria produce outer membrane-enclosed tubes in unstructured environments. J. Bacteriol. *196*, 1807–1814.